ACS OMEGA

http://pubs.acs.org/journal/acsodf

Article

Solid-State Fluorescent Selenium Quantum Dots by a Solvothermal-Assisted Sol–Gel Route for Curcumin Sensing

Kuttappan Anupama, Tessy Paul, and Kakkassery Aippunny Ann Mary*

Cite This: *ACS Omega* 2021, 6, 21525–21533

Read Online

ACCESS | Metrics & More | Article Recommendations | Supporting Information

ABSTRACT: Toward the need for solid-state fluorescent quantum dots, resistant to self-quenching, we describe a solvothermal-assisted sol–gel method to synthesize Se quantum dots. Morphological and crystalline characterizations reveal that Se quantum dots (average size 3–8 nm) have a trigonal crystal structure. The presence of planar defects (dislocations, stacking faults, twins, and grain boundaries) suggests formation of Se nanocrystallites through aggregation-based crystal growth mechanisms. Under ultraviolet excitation, the quantum dots exhibit an excitation wavelength-dependent solid-state blue emission with an average lifetime of 1.96 ns. Depending on fluorescence quenching by curcumin, selenium quantum dots act as ideal candidates for inner filter effect-based curcumin sensing.

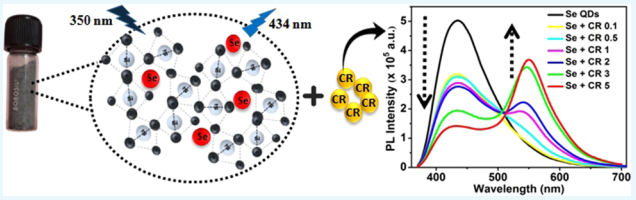

INTRODUCTION

Nanomaterials have been an intriguing subject of research for the last several decades as their physical properties can be drastically changed by tailor-made structural and morphological modifications. The presence of discrete energy states, tunable band gaps, and enhanced fluorescent properties makes elemental quantum dots (QDs) promising candidates compared to their one-dimensional (1D) or two-dimensional (2D) counterparts. More recently, fluorescent quantum dots of graphene,[1] phosphorous,[2] boron,[3] selenium,[4] etc., have attracted increased attention because of their intrinsic fluorescent properties, making them promising candidates for development of biosensing and bioimaging platforms. Among them, selenium holds an inimitable position at the boundary of group VI in the periodic table between van der Waals molecular solids (O_2 and S_8) and the covalent solid Te. It can exist in several solid modifications: two monoclinic (α and β), the most stable trigonal form, one cubic, and one amorphous modification.[5] Prior studies widely focused on amorphous Se (a-Se) nanoparticles and trigonal Se (t-Se) nanowires due to their ease of formation and stability.[6−9] Dependence of ultrafast optical nonlinearity on the cubic and amorphous forms of Se quantum dots is studied in silica xerogels prepared through a simple sol–gel route.[5] Although some progress has been achieved in the synthesis of t-Se nanoparticles[7,10,11] through green assisted synthesis as well as precursor conversion methods, synthesis of t-Se quantum dots has not been equally explored. Recently, t-Se QDs have been synthesized by ultrasound liquid-phase exfoliation (LPE) of $NbSe_2$ powders using *N*-methyl-2-pyrrolidone (NMP) as the dispersant.[12] Photocarrier dynamics and pathways involved in t-Se QDs synthesized by a similar LPE method were also studied in a very recent work.[13] Research efforts are increasing progressively to explore simple methods to synthesize different Se QD allotropes. Moreover, considering the influence of crystal defects on the physical properties of a material, it is crucial to understand the growth mechanism and microstructure of Se QDs, which are not yet well explored.

Among all of the polyphenolic components of turmeric, curcumin (CR) possesses exceptional biological and pharmacological properties.[14] It is widely used as a nutraceutical in food and both as a colorant and a condiment. Although utilized for its antibacterial,[15] anti-inflammatory,[16] antioxidant,[17] and hepatoprotective properties,[18] curcumin shows good inhibitory effects toward certain carcinogens.[19,20] It is used in clinical medicine for the treatment of various diseases like arthritis, cystic fibrosis,[21] cardiovascular diseases,[22] Alzheimer's,[23] and even HIV.[24] However, studies suggest that an excessive dose of curcumin can impose higher oxidative stress, resulting in chromosomal aberrations to the mitochondria and nuclear genomes in human hepatoma G2 cells.[25] Moreover, it decreases intracellular ATP levels, triggering the necrosis process.[26] Owing to its wide importance and medicinal value, it is highly essential to monitor the level of curcumin in foods and medications through a reliable, fast, and sensitive route. To date, various analytical assays have been reported for the detection of curcumin including high-performance liquid chromatography,[27] voltammetry,[28] electrochemical methods,[29]

Received: May 9, 2021
Accepted: July 28, 2021
Published: August 10, 2021

capillary electrophoresis,[30] spectrophotometry,[31] resonance light scattering,[32] and spectrofluorimetry.[33,34] Although many of these are highly sensitive and quantitative techniques, their high capital and maintenance expenses have turned the attention of researchers toward sensitive, quickly responsive, and cost-effective fluorescence sensing. Recently, various fluorophores such as P-, N-, B-codoped carbon quantum dots,[35] Mn-doped ZnS QDs,[36] graphitic carbon nitrides,[37] etc., have been explored as fluorescent nanosensors for quantitative determination of curcumin. However, QDs tend to lose their fluorescence properties in aqueous and solid states due to irreversible photobleaching or aggregation-induced luminescence quenching.[38,39] This limits their practical applicability in designing sensors and imaging devices where materials with solid-state fluorescence are inevitable. Till now, research efforts on Se QDs have rarely focused on solid-state fluorescence and their biosensing applications.

Herein, a facile solvothermal route is developed for in situ synthesis of Se quantum dots in a SiO_2 matrix. In solid mesoporous silica, collision and aggregation of Se QDs can rarely happen, preventing them from degradation and surface oxidation. This gives a longer shelf life, making them ideal candidates for solid-state fluorescence and optoelectronic applications. This stable solid-state fluorescence obtained from Se QDs is explored for quantitative determination of curcumin.

RESULTS AND DISCUSSION

The powder X-ray diffraction (p-XRD) pattern of Se−SiO_2 composites with different Se contents is shown in Figure S1. It can be inferred that all Se−SiO_2 composites have the same crystal structure as peak positions in the p-XRD pattern remain the same and their intensities increase with Se contents. As shown in Figure 1, the occurrence of diffraction peaks at

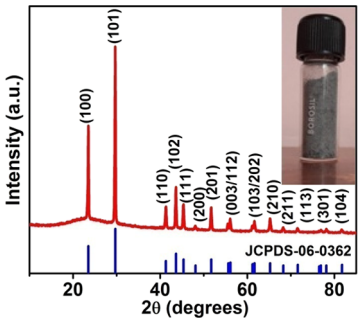

Figure 1. XRD pattern of the 40 wt % Se−SiO_2 composite. The inset shows its digital photograph under visible light.

different positions can be indexed to hexagonal Se (JCPDS code: 06-0362) and no impurity peaks are detected. The broad spectrum peaked at the 2θ value of 23° in the p-XRD pattern can be ascribed to the presence of amorphous SiO_2. The inset of Figure 1 shows a photograph of the 40 wt % Se−SiO_2 nanocomposite.

The field emission scanning electron microscopy (FESEM) image (Figure 2a) of the Se−silica nanocomposite shows fused distorted ellipsoid-like structures with average length in the range of 80−190 nm and diameters ranging from 60 to 120 nm. The large field transmission electron microscopy (TEM) image displayed in Figure 2b clearly illustrates the same morphology of the Se−silica nanocomposite. The average length and breadth of the microstructures are calculated as 130 and 110 nm, respectively. Moreover, on close examination, it can be inferred that each ellipsoid-like structure consists of many homogeneously distributed quasi-spherical Se quantum dots with a very narrow size distribution.

The high-resolution TEM (HRTEM) image shows approximately spherical t-Se QDs distributed evenly without obvious aggregation (Figure 3a). The size of nanocrystallites is in the range of 3−8 nm as obtained from a size distribution histogram (inset of Figure 3a). On closer examination, it can be observed that the synthesized t-Se QDs (Figure 3b) exhibit randomly oriented crystallites with abrupt disordered edges having considerable grain boundary defects. Clear lattice fringes revealed the excellent crystalline nature of t-Se QDs. The interplanar distances of 3.02, 2.15, 2.03, 1.95, and 1.75 Å can be assigned to the (101), (110), (102), (111), and (201) planes of trigonal Se, respectively. Upon deeper investigation, it can be inferred that like many nanocrystallites in the system, t-Se QDs possess a considerable number of planar defects. Figure 3c shows the presence of stacking faults (SF), edge dislocations (ED), and twins (T), which are depicted in Figure 3d. This can be attributed to the aggregation-based crystal growth mechanism involved in the synthesis. During hydrothermal coarsening, adjacent primary particles in the solution collide and coalesce, resulting in secondary particles. This spontaneous self-organization following a common crystallographic orientation and imperfect particle attachment often leads to line and planar defects.[40]

Recently, the growth and formation of t-Se nanotubes were investigated in detail and explained through different crystal growth mechanisms.[41−43] For ultrasonic, hydrothermal, and surfactant-assisted synthesis methods, crystal growth is mediated through the ultrasonic-assisted oriented attachment (OA) growth mechanism,[41] surfactant-directed growth mechanism,[42] and nucleation−dissolution−recrystallization[43] mechanism, respectively. As observed from HRTEM images, the oriented attachment (OA)-based growth mechanism of trigonal Se QDs can be explained by analyzing the nanocrystallites with irregular shapes and abrupt edges. The presence of lattice defects (grain boundaries, twins, and stacking faults), a clear coalescence profile, and the peculiar structures of primary nanocrystals is due to aggregation of primary crystallites by sharing a common crystallographic orientation. Under solvothermal conditions, the decomposition of selenous acid is followed by nucleation of trigonal selenium nanocrystallites at favorable sites of tetraethyl orthosilicate (TEOS). The strong surface adsorption of TEOS promotes the initial growth of nanocrystals through the pure OA mechanism. This slows down the dissolution of particles in solution, and the nucleation−dissolution−recrystallization mechanism is thermodynamically prohibited. The solvothermal treatment of the mixture triggers rapid hydrolysis of TEOS in the presence of water and ethanol. This is simultaneously followed by a cascade of quick polycondensation reactions during which the growth of trigonal Se QDs is promoted at preferred sites. Although crystallization of anisotropic trigonal Se is promoted by the OA-assisted mechanism, the SiO_2 network inhibits their further characteristic growth to 1D nanostructures. The capping effect of the SiO_2 network acts as a growth-controlling agent, and the product retains a quasi-spherical shape with abrupt edges. Scheme 1 represents the aforesaid mechanism of formation of t-Se quantum dots.

https://doi.org/10.1021/acsomega.1c02441
ACS Omega 2021, 6, 21525−21533

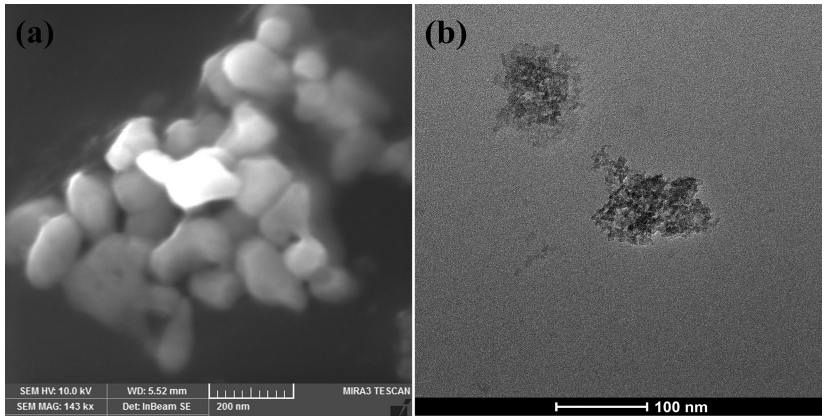

Figure 2. (a) FESEM and (b) TEM images of the Se−silica nanocomposite.

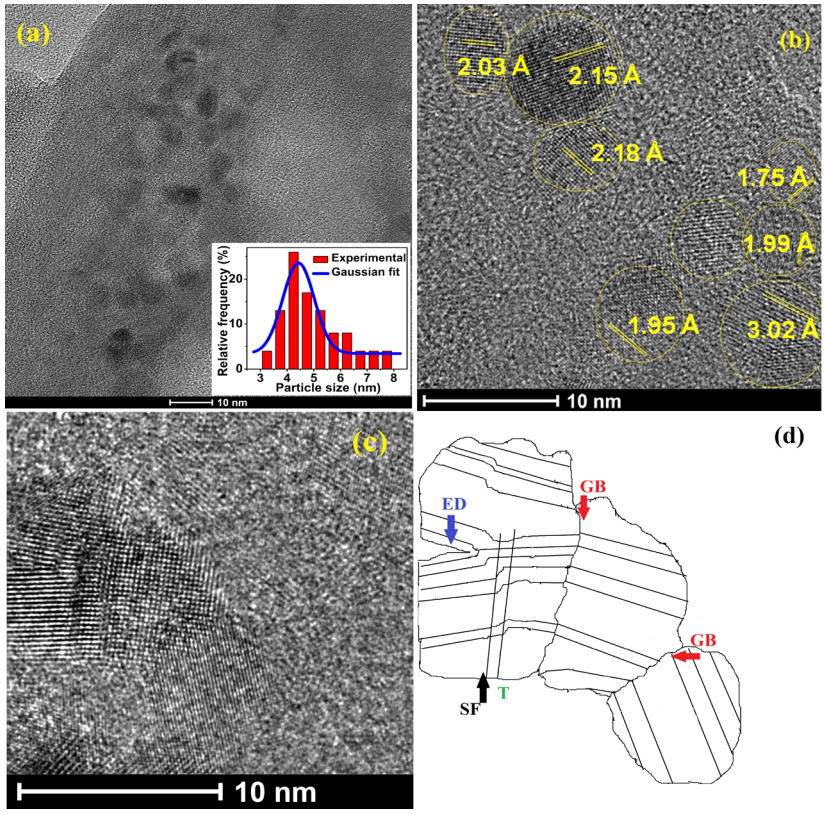

Figure 3. (a) Large-area HRTEM image of the Se−SiO_2 composite (inset shows the particle size distribution of Se QDs). (b, c) HRTEM image of t-Se QDs showing *d* spacings. (d) Edge dislocation (ED), stacking fault (SF), twin (T), and grain boundaries (GB) in the crystallites as observed from HRTEM.

Scheme 1. Mechanism of Formation of t-Se QDs in Silica by a Solvothermal-Assisted Sol−Gel Route

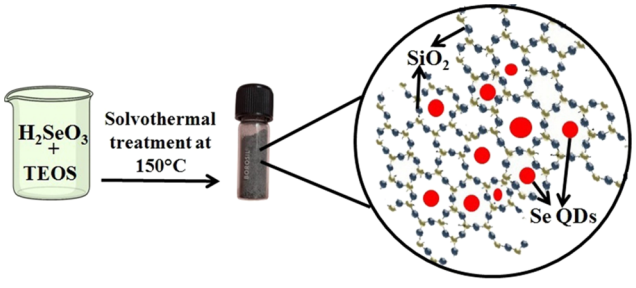

The Raman spectrum (Figure 4) of t-Se QDs shows a single resonance peak at 237 cm^{-1}, which can be attributed to the stretching vibrations of helical selenium chains (A_1).[44] This confirms the formation of well-crystallized trigonal Se QDs as observed from XRD and HRTEM. The absence of characteristic Raman resonance absorption bands centered at 256 cm^{-1} for monoclinic Se and at 264 cm^{-1} for amorphous Se indicates the phase purity of the composite.[45]

From the Fourier transform infrared (FTIR) spectrum of the t-Se−SiO_2 composite (Figure 5a), the observed peak values are in good agreement with the reported data for SiO_2-based materials.[46] The characteristic bands observed at 784 and 1054 cm^{-1} can be attributed to Si−O−Si symmetric stretching and bending vibrations. The existence of an oxoethyl group is

https://doi.org/10.1021/acsomega.1c02441
ACS Omega 2021, 6, 21525−21533

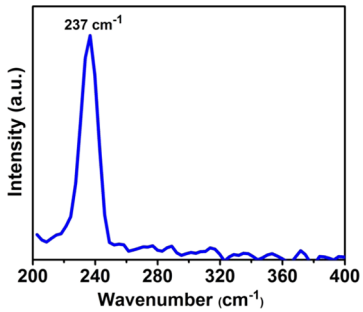

Figure 4. Raman spectrum of t-Se QDs.

indicated by the weak absorption bands at 1637 and 972 cm^{-1}. The broad absorption around 3354 cm^{-1} depicts the stretching vibrations of H-bonded silanols with water (hydroxyl group).[47,48] The peak at 549 cm^{-1} is associated with four-membered siloxane ring vibrations of the matrix. From the differential scanning calorimetry (DSC) curve (Figure 5b), the sharp endothermic peak at 112.54 °C can be attributed to the presence of moisture and other organic solvents in the Se−Silica composite.[49] The dip observed at 221.45 °C can be assigned to the melting point of trigonal Se (~221 °C).[50] The absence of DSC thermogram peaks corresponding to the monoclinic (~175 °C) and amorphous (~70 °C) forms reaffirms the homogeneity and purity of the prepared composite.[51] The melting enthalpy value of t-Se QDs obtained as 2.672 J/g is considerably lower than those of selenium nanoparticles.[52−54] This can be attributed to the dependence of size on the melting thermodynamics of the material.[53] Going from bulk to quantum dots, there is an increase in the surface area-to-volume ratio, thereby increasing the surface energy. Hence, the melting process is carried out with the contribution from surface enthalpy, which reduces the melting enthalpy.[53]

The UV−visible absorption spectrum of t-Se quantum dots shows broad absorption in the lower wavelength region (Figure 6a), and an absorption edge is observed around 750 nm. Some previous studies available in the literature show that trigonal Se nanowires have weak absorption maxima at 346, 450, and 570 nm.[55] The semimetallic nature of the material and structural similarities with the bulk cause broadening of these individual peaks.[56] The optical band gap of t-Se QDs is 1.64 eV as calculated from a Tauc plot (inset of Figure 6a). According to values reported in the literature, trigonal selenium exhibits a band gap energy value of 2 eV.[13,57,58] Although a higher energy gap is expected in quantum dots due to confinement effects, a slight decrease in band gap is observed in t-Se QDs. This can be attributed to the presence of surface states and traps.[59,60] Microstructural studies indicate the presence of surface states and defects. Due to the smaller size of nanocrystallites, a higher proportion of the total number of atoms will be located on the surface. Moreover, nanocrystallites have abrupt edges and imperfect surfaces. Therefore, there will be a large density of surface states, which act as active electron and/or hole traps upon optical excitation. The excited carriers undergo nonradiative recombination and no band edge emission was observed for t-Se QDs, consistent with the results obtained by Jiang et al.[13] Under a UV excitation wavelength of 350 nm, the t-Se−SiO_2 composite exhibits a blue emission peaked at a wavelength of 434 nm (Figure 6b). This can be assigned to direct interband radiative recombination in t-Se QDs.[13] Due to spin−orbit coupling, the valence band and conduction band might undergo energy splitting and radiative recombination of carriers can happen in the same *k*-space between energy bands. From normalized PL spectra, it is clear that the emission wavelength shifts from 418 to 449 nm when the excitation wavelength varies from 320 to 370 nm (inset of Figure 6b). The observed red shift in the emission peak suggests that the prepared QDs possess excitation wavelength-dependent emission, which is consistent with reported data.[12] The quantum yield (QY) for t-Se QDs is obtained as ~0.13%. This low value of room-temperature photoluminescence QY is due to the high defect density in the material, which is consistent with HRTEM and UV−visible absorption data. The defect-mediated nonradiative recombination from surface states and trap sites outnumbers the number of photons emitted, which results in the reduced QY.[61] Similar quantum yield values have been reported for certain metal nanoclusters (NCs)[62] and some two-dimensional (2D) transition-metal dichalcogenides like MoS_2[63] due to the presence of surface states and defects.

Fluorescence Detection of Food Dyes. To examine the sensing ability of the t-Se−SiO_2 composite for curcumin, steady-state fluorescence emission spectra of t-Se QDs (0.2 g) were closely monitored (Figure 7a) with different concentrations of curcumin (0−5 wt %). It can be observed that the fluorescence intensity of t-Se QDs is decreased distinctly upon addition of curcumin. Moreover, an increase in curcumin content results in the occurrence of a new emission band peaked at 550 nm wavelength. The enhanced characteristic yellow emission of curcumin indicates the transfer of photon energy between curcumin and t-Se QDs. The ratio of fluorescence intensities peaked at 550 and 434 nm wavelengths

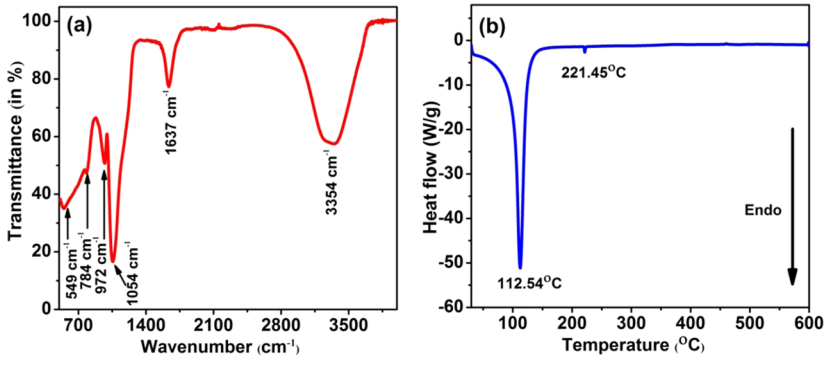

Figure 5. (a) FTIR spectrum and (b) DSC measurements of the t-Se−SiO_2 composite.

https://doi.org/10.1021/acsomega.1c02441
ACS Omega 2021, 6, 21525−21533

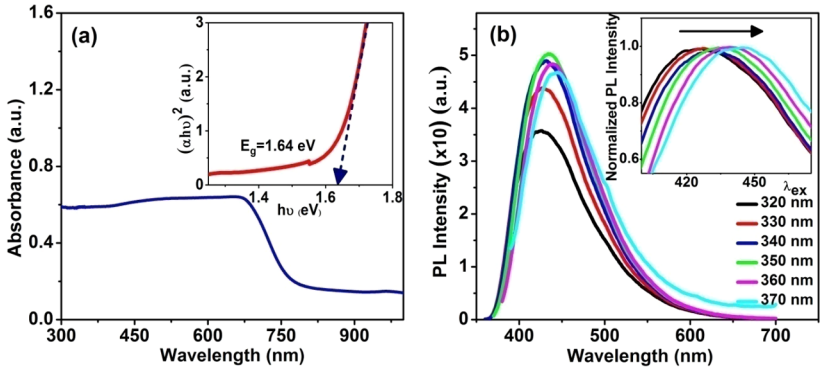

Figure 6. (a) UV−visible absorption spectrum of the t-Se−SiO_2 composite; the Tauc plot (inset) gives the optical band gap as 1.64 eV. (b) Photoluminescence spectra measured in the t-Se−SiO_2 composite with varying λ_{ex} from 320 to 370 nm. Normalized PL spectra (inset) show excitation-dependent emission.

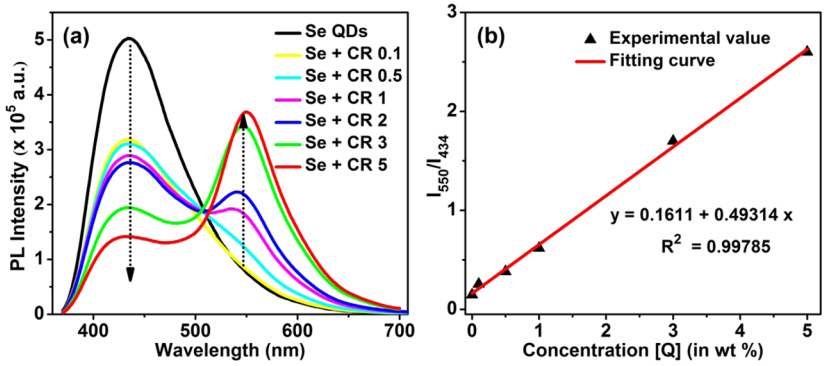

Figure 7. (a) Fluorescence responses of t-Se QDs in the presence of varying concentrations (wt %) of curcumin (from top: 0, 0.1, 0.5, 1, 2, 3, and 5 wt %). (b) Plot of the fluorescence intensity ratio (I_{550}/I_{434}) as a function of curcumin concentration.

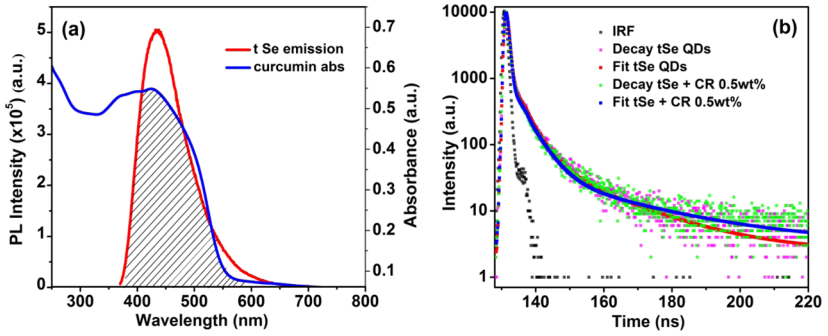

Figure 8. (a) UV−vis absorption spectrum of curcumin and emission spectrum of t-Se QDs showing spectral overlap. (b) Fluorescence decay curves of t-Se QDs and t-Se QDs−curcumin..

(I_{550}/I_{434}) shows a satisfactory linear relationship (Figure 7b) as the concentration of the analyte varies from 0 to 5 wt % (~0 to 10.52 mg). The calibration equation is as follows

$$I(550)/I(434) = 0.1611 + 0.49314[Q]$$

where $I(434)$ and $I(550)$ are the fluorescence intensities of emission bands at λ_{ex} of 350 nm and [Q] represents the concentration of curcumin. The limit of detection (LOD) was calculated to be 0.09 wt % (~180 μg) with LOD = 3 σ/S, where σ represents the standard deviation of the pure Se QDs for N = 3 and S is the slope of the calibration curve. The obtained value of R^2 = 0.99785 indicates excellent linearity. To assess the selectivity of the system toward curcumin, relative fluorescence responses (I_{550}/I_{434}) of the t-Se−SiO_2 composite toward interfering analytes like aspartic acid, alanine, arginine, glutamic acid, glycine, histidine, lysine, sucrose, fructose, valine, glucose, and curcumin were analyzed. It is clear that only addition of curcumin makes a remarkable change in the I_{550}/I_{434} value (Figure S2).

Mechanism of Quenching. From Figure 8a, it can be observed that the broad absorption of curcumin in the short wavelength region has considerable overlap with the emission spectrum of t-Se QDs. This clearly indicates that the decrease in fluorescence of t-Se QDs upon addition of curcumin is due to electron transfer, energy transfer, or the inner filter effect (IFE).[35,64−68] As curcumin is negatively charged, there will be no electrostatic interaction between selenium QDs and curcumin.[35,69] Thus, the fluorescence quenching observed in the mixture is not due to the electron transfer mechanism. UV−visible absorption spectra of t-Se QDs, Se−curcumin, and

https://doi.org/10.1021/acsomega.1c02441
ACS Omega 2021, 6, 21525−21533

Table 1. Fluorescence Lifetime Parameters of t-Se in the Absence and Presence of Curcumin

curcumin (wt %)	τ_1 (ns)	a_1	τ_2 (ns)	a_2	τ_3 (ns)	a_3	τ_{avg} (ns)	χ^2
0	4.10	17.75	19.26	5.41	0.25	76.83	1.96	1.31
0.5	4.41	16.46	27.07	4.20	0.23	79.34	2.04	1.32

curcumin are shown in Figure S3, and no additional peak can be observed in the Se−curcumin spectrum. This eliminates any possible complex formation between Se and curcumin which suggests that the possible quenching mechanism observed in Se−curcumin is the IFE. The enhanced emission peaked at the 550 nm wavelength observed for the t-Se−SiO_2−curcumin compared to the SiO_2−curcumin mixture illustrates the transfer of photon energy between curcumin and t-Se QDs (Figure S4). To confirm the aforementioned quenching mechanism, time-resolved fluorescence lifetime decay measurements were carried out at an excitation wavelength of 340 nm (Figure 8b). The fluorescence data was reliably fitted using a tri-exponential decay function

$$I(t) = I(0) + \sum A_i \times e^{(-\frac{t}{\tau i})}$$

where τ_i represents the lifetime, A_i denotes the relative amplitude of the decay process, while $I(0)$ and $I(t)$ refer to the fluorescence intensities at 0 and t, respectively.[70] The fitting parameters obtained are shown in Table 1. The average lifetime of t-Se QDs remains unchanged upon addition of 0.5 wt % curcumin. This implies that the excited fluorophore decays in its native natural lifetime and is not in any way bound to the analyte. This confirms the fluorescence quenching mechanism of t-Se QDs as the IFE without any chemical link between donor and acceptor systems. The results suggest that solid-state fluorescence from t-Se QDs can be well applied to less costly IFE-based practical fluorescence sensors.

CONCLUSIONS

In summary, t-Se QDs in silica were synthesized using a solvothermal-assisted rapid hydrolysis and polycondensation route. A structural evaluation of the as-synthesized Se−silica nanocomposites confirms the formation of trigonal Se QDs−SiO_2 composites. From HRTEM images, nanocrystallites with considerable planar defects were observed, and the oriented attachment (OA)-based crystal growth mechanism was discussed in detail. The lower band gap value of 1.64 eV calculated from UV−vis absorption measurements can be attributed to the presence of surface states and traps. The blue emission observed for t-Se QDs under UV excitation was successfully utilized for the sensitive detection of curcumin. To the best of our knowledge, reports on solid-state fluorescence in trigonal Se QDs are not readily available in the literature. The decrease in fluorescence intensity of t-Se QDs in the presence of curcumin was due to the IFE-based quenching mechanism, which has significant applications toward designing instrument-free practical fluorescence sensors.

EXPERIMENTAL SECTION

Materials. Tetraethyl orthosilicate (TEOS) ($Si(OC_2H_5)_4$, 98%), selenous acid (H_2SeO_3, 98%), and curcumin ($[HOC_6H_3(OCH_3)CH{=}CHCO]_2CH_2$ from *Curcuma longa* (turmeric) powder) were procured from Sigma-Aldrich. Distilled water was used throughout the experiment.

Apparatus and Characterization. The crystallinity of the sample was observed using a benchtop powder X-ray diffractometer (Aeris Research, PANalytical, The Netherlands) with a scanning range of $2\theta = 10-90°$ with Cu Kα radiation (λ = 1.540598 Å). Morphological parameters were evaluated from field emission scanning electron microscopy (FESEM) images recorded on a TESCAN MIRA3 LMH and high-resolution transmission electron microscopy (HRTEM) data using a TALOS F200S G2 transmission electron microscope (200 kV, FEG, CMOS Camera 4K × 4K). Raman spectra obtained from a Horiba Jobin Yvon T64000 Raman spectrometer were used for phase identification. Structural analysis was carried out using Fourier transform infrared (FTIR) spectra in the region 400−4000 cm^{-1} obtained from an FTIR spectrometer (Thermo Nicolet, USA) at room temperature. Thermal analysis was performed using a differential scanning calorimeter (TA Instruments, Germany) in the temperature range 30−600 °C at a heating rate of 10 °C/min. The absorption spectra in the entire visible range were recorded on a UV−vis spectrophotometer (Jasco, Japan). All fluorescence measurements were recorded on a Fluorolog NIR spectrofluorometer (Horiba Jobin Yvon, USA). Decay lifetimes were evaluated using a time-resolved Fluorimax fluorimeter (Horiba Jobin Yvon, USA).

Synthesis of the Se−Silica Composite. Se (10, 20, 30, and 40 wt %) in 2 g of silica was prepared by a simple solvothermal route through rapid hydrolysis, condensation, and polymerization of tetraethyl orthosilicate (TEOS) in the presence of ethanol and distilled water. An aqueous solution of selenous acid was added to TEOS and ethanol at room temperature. The precursor molar ratio of selenium to silica was fixed at 1:2, 1:3, 1:5, and 1:11 for the synthesis of 40, 30, 20, and 10 wt % Se−silica nanocomposite, respectively. Two drops of 1 M HNO_3 was added as a catalyst. The resulting mixture was stirred continuously for 1 h to obtain a clear solution. The molar ratio of TEOS−water−ethanol was taken as 1:2:2. The solution was then poured into a 50 mL Teflon-lined autoclave and heated at 150 °C for 24 h. The gray-colored composite obtained was powdered and used for further characterizations.

Determination of Curcumin. For quantitative determination of curcumin in different systems, 0.2 g of 40 wt % Se−SiO_2 was added to varying concentrations (wt %) of chloroform solutions of curcumin (10 mL). The solution was then centrifuged and washed with an excess of solvent to remove the loosely bound residues. The mixture was then dried, and the optical properties of the slightly yellowish powder obtained were investigated by fluorescence spectroscopy.

ASSOCIATED CONTENT

Supporting Information

The Supporting Information is available free of charge at https://pubs.acs.org/doi/10.1021/acsomega.1c02441.

The XRD pattern of Se−SiO_2 composites with different Se contents; relative fluorescence response (I_{550}/I_{434}) of the probe toward 1 wt % interferents like aspartic acid, alanine, arginine, glutamic acid, glycine, histidine, lysine, sucrose, fructose, valine, glucose, and curcumin; UV−vis

https://doi.org/10.1021/acsomega.1c02441
ACS Omega 2021, 6, 21525−21533

spectra of t-Se QDs, curcumin, and t-Se QD + curcumin; photoluminescence spectra of t-Se−SiO_2−curcumin and SiO_2-curcumin mixture having same curcumin contents (0.5 wt%) (PDF)

AUTHOR INFORMATION

Corresponding Author

Kakkassery Aippunny Ann Mary − *Department of Physics, St. Thomas' College (Autonomous), Thrissur 680001 Kerala, India;* orcid.org/0000-0002-2746-1830; Email: annmaryka@stthomas.ac.in

Authors

Kuttappan Anupama − *Department of Physics, St. Thomas' College (Autonomous), Thrissur 680001 Kerala, India*

Tessy Paul − *Department of Physics, St. Thomas' College (Autonomous), Thrissur 680001 Kerala, India*

Complete contact information is available at: https://pubs.acs.org/10.1021/acsomega.1c02441

Notes

The authors declare no competing financial interest.

ACKNOWLEDGMENTS

This work was financially supported by the Kerala State Council for Science Technology and Environment (KSCSTE). The authors gratefully acknowledges the XRD Facility, funded by College with Potential for Excellence (CPE)- UGC at St. Thomas' College (Autonomous), Thrissur. The authors thank the School of Pure and Applied Physics and DST—Sophisticated Analytical Instrument Facility (SAIF), MG University, Kottayam, Kerala, for the facilities and services provided. The authors also thank the TEM Facility, funded by a TPF Nanomission, GoI Project, at the Centre for Nano and Soft Matter Sciences, Bengaluru.

REFERENCES

(1) Yan, X.; Song, Y.; Zhu, C.; Song, J.; Du, D.; Su, X.; Lin, Y. Graphene Quantum Dot−MnO2 Nanosheet Based Optical Sensing Platform: A Sensitive Fluorescence "Turn Off−On" Nanosensor for Glutathione Detection and Intracellular Imaging. *ACS Appl. Mater. Interfaces* **2016**, *8*, 21990−21996.

(2) Li, Y.; Liu, Z.; Hou, Y.; Yang, G.; Fei, X.; Zhao, H.; Guo, Y.; Su, C.; Wang, Z.; Zhong, H.; Zhuang, Z.; Guo, Z. Multifunctional Nanoplatform Based on Black Phosphorus Quantum Dots for Bioimaging and Photodynamic/Photothermal Synergistic Cancer Therapy. *ACS Appl. Mater. Interfaces* **2017**, *9*, 25098−25106.

(3) Huo, B.; Liu, B.; Chen, T.; Cui, L.; Xu, G.; Liu, M.; Liu, J. One-Step Synthesis of Fluorescent Boron Nitride Quantum Dots via a Hydrothermal Strategy Using Melamine as Nitrogen Source for the Detection of Ferric Ions. *Langmuir* **2017**, *33*, 10673−10678.

(4) Zhu, M.-L.; Gao, Z.-T.; Lu, J.-X.; Wang, Y.; Wang, G.; Qiu, Y.; Liu, T.-H.; Zhu, C.-N.; Wang, S.-X.; Li, P.; Yang, L. *Amorphous Nano-Selenium Quantum Dots Prevent Pulmonary Arterial Hypertension Through Recoupling Endothelial Nitric Oxide Synthase*, SSRN Scholarly Paper ID 3539637; Social Science Research Network: Rochester, NY, 2020.

(5) Ann Mary, K. A.; Unnikrishnan, N. V.; Philip, R. Cubic to Amorphous Transformation of Se in Silica with Improved Ultrafast Optical Nonlinearity. *RSC Adv.* **2015**, *5*, 14034−14041.

(6) Mondal, K.; Roy, P.; Srivastava, S. K. Facile Biomolecule-Assisted Hydrothermal Synthesis of Trigonal Selenium Microrods. *Cryst. Growth Des.* **2008**, *8*, 1580−1584.

(7) Zhang, J.; Fu, Q.; Xue, Y.; Cui, Z. Controlled Synthesis of T-Se Nanomaterials with Various Morphologies via a Precursor Conversion Method. *CrystEngComm* **2018**, *20*, 1220−1231.

(8) Gates, B.; Mayers, B.; Cattle, B.; Xia, Y. Synthesis and Characterization of Uniform Nanowires of Trigonal Selenium. *Adv. Funct. Mater.* **2002**, *12*, 219−227.

(9) Liu, L.; Peng, Q.; Li, Y. Preparation of Monodisperse Se Colloid Spheres and Se Nanowires Using Na2SeSO3 as Precursor. *Nano Res.* **2008**, *1*, 403−411.

(10) Kokila, K.; Elavarasan, N.; Sujatha, V. Diospyros Montana Leaf Extract-Mediated Synthesis of Selenium Nanoparticles and Their Biological Applications. *New J. Chem.* **2017**, *41*, 7481−7490.

(11) Prasad, K. S.; Selvaraj, K. Biogenic Synthesis of Selenium Nanoparticles and Their Effect on As(III)-Induced Toxicity on Human Lymphocytes. *Biol. Trace Elem. Res.* **2014**, *157*, 275−283.

(12) Qian, F.; Li, X.; Tang, L.; Lai, S. K.; Lu, C.; Lau, S. P. Selenium Quantum Dots: Preparation, Structure, and Properties. *Appl. Phys. Lett.* **2017**, *110*, No. 053104.

(13) Jiang, X.; Huang, W.; Wang, R.; Li, H.; Xia, X.; Zhao, X.; Hu, L.; Chen, T.; Tang, Y.; Zhang, H. Photocarrier Relaxation Pathways in Selenium Quantum Dots and Their Application in UV-Vis Photodetection. *Nanoscale* **2020**, *12*, 11232−11241.

(14) Tønnesen, H. H.; Karlsen, J.; Adhikary, S. R.; Pandey, R. Studies on Curcumin and Curcuminoids XVII. Variation in the Content of Curcuminoids InCurcuma Longa L. from Nenal during One Season. *Z. Lebensm.-Unters. Forsch.* **1989**, *189*, 116−118.

(15) Wang, Y.; Lu, Z.; Wu, H.; Lv, F. Study on the Antibiotic Activity of Microcapsule Curcumin against Foodborne Pathogens. *Int. J. Food Microbiol.* **2009**, *136*, 71−74.

(16) Bereswill, S.; Muñoz, M.; Fischer, A.; Plickert, R.; Haag, L.-M.; Otto, B.; Kühl, A. A.; Loddenkemper, C.; Göbel, U. B.; Heimesaat, M. M. Anti-Inflammatory Effects of Resveratrol, Curcumin and Simvastatin in Acute Small Intestinal Inflammation. *PLoS One* **2010**, *5*, No. e15099.

(17) Menon, V. P.; Sudheer, A. R. Antioxidant and Anti-Inflammatory Properties of Curcumin. In *The Molecular Targets and Therapeutic Uses of Curcumin in Health and Disease*; Aggarwal, B. B.; Surh, Y.-J.; Shishodia, S., Eds.; Advances in Experimental Medicine and Biology, Springer: Boston, MA, 2007; pp 105−125.

(18) Girish, C.; Koner, B. C.; Jayanthi, S.; Rao, K. R.; Rajesh, B.; Pradhan, S. C. Hepatoprotective Activity of Picroliv, Curcumin and Ellagic Acid Compared to Silymarin on Paracetamol Induced Liver Toxicity in Mice. *Fundam. Clin. Pharmacol.* **2009**, *23*, 735−745.

(19) Goel, A.; Kunnumakkara, A. B.; Aggarwal, B. B. Curcumin as "Curecumin": From Kitchen to Clinic. *Biochem. Pharmacol.* **2008**, *75*, 787−809.

(20) Lin, L.; Shi, Q.; Nyarko, A. K.; Bastow, K. F.; Wu, C.-C.; Su, C.-Y.; Shih, C. C.-Y.; Lee, K.-H. Antitumor Agents. 250. Design and Synthesis of New Curcumin Analogues as Potential Anti-Prostate Cancer Agents. *J. Med. Chem.* **2006**, *49*, 3963−3972.

(21) Mouslmani, M.; M Rosenholm, J.; Prabhakar, N.; Peurla, M.; Baydoun, E.; Patra, D. Curcumin Associated Poly(Allylamine Hydrochloride)-Phosphate Self-Assembled Hierarchically Ordered Nanocapsules: Size Dependent Investigation on Release and DPPH Scavenging Activity of Curcumin. *RSC Adv.* **2015**, *5*, 18740−18750.

(22) Aggarwal, B. B.; Harikumar, K. B. Potential Therapeutic Effects of Curcumin, the Anti-Inflammatory Agent, against Neurodegenerative, Cardiovascular, Pulmonary, Metabolic, Autoimmune and Neoplastic Diseases. *Int. J. Biochem. Cell Biol.* **2009**, *41*, 40−59.

(23) Hamaguchi, T.; Ono, K.; Yamada, M. REVIEW: Curcumin and Alzheimer's Disease. *CNS Neurosci. Ther.* **2010**, *16*, 285−297.

(24) Prasad, S.; Tyagi, A. K. Curcumin and Its Analogues: A Potential Natural Compound against HIV Infection and AIDS. *Food Funct.* **2015**, *6*, 3412−3419.

(25) Cao, J.; Jia, L.; Zhou, H.-M.; Liu, Y.; Zhong, L.-F. Mitochondrial and Nuclear DNA Damage Induced by Curcumin in Human Hepatoma G2 Cells. *Toxicol. Sci.* **2006**, *91*, 476−483.

(26) Chan, W.-H.; Wu, H.-Y.; Chang, W. H. Dosage Effects of Curcumin on Cell Death Types in a Human Osteoblast Cell Line. *Food Chem. Toxicol.* **2006**, *44*, 1362−1371.
(27) Jayaprakasha, G. K.; Jagan Mohan Rao, L.; Sakariah, K. K. Improved HPLC Method for the Determination of Curcumin, Demethoxycurcumin, and Bisdemethoxycurcumin. *J. Agric. Food Chem.* **2002**, *50*, 3668−3672.
(28) Chaisiwamongkhol, K.; Ngamchuea, K.; Batchelor-McAuley, C.; Compton, R. G. Multiwalled Carbon Nanotube Modified Electrodes for the Adsorptive Stripping Voltammetric Determination and Quantification of Curcumin in Turmeric. *Electroanalysis* **2017**, *29*, 1049−1055.
(29) Kotan, G.; Kardaş, F.; Yokuş, ÖA.; Akyıldırım, O.; Saral, H.; Eren, T.; Yola, M. L.; Atar, N. A Novel Determination of Curcumin via Ru@Au Nanoparticle Decorated Nitrogen and Sulfur-Function-alized Reduced Graphene Oxide Nanomaterials. *Anal. Methods* **2016**, *8*, 401−408.
(30) Sun, X.; Gao, C.; Cao, W.; Yang, X.; Wang, E. Capillary Electrophoresis with Amperometric Detection of Curcumin in Chinese Herbal Medicine Pretreated by Solid-Phase Extraction. *J. Chromatogr. A* **2002**, *962*, 117−125.
(31) Tang, B.; Ma, L.; Wang, H.; Zhang, G. Study on the Supramolecular Interaction of Curcumin and β-Cyclodextrin by Spectrophotometry and Its Analytical Application. *J. Agric. Food Chem.* **2002**, *50*, 1355−1361.
(32) Chen, X.; Liang, S.; Zhu, L.; Liu, J.; Zhang, G.; Chen, Z. High-Sensitivity Determination of Curcumin in Human Urine Using Gemini Zwitterionic Surfactant as a Probe by Resonance Light Scattering Technique. *Phytochem. Anal.* **2012**, *23*, 456−461.
(33) Wang, F.; Huang, W.; Wang, Y. Fluorescence Enhancement Effect for the Determination of Curcumin with Yttrium(III)—Curcumin—Sodium Dodecyl Benzene Sulfonate System. *J. Lumin.* **2008**, *128*, 110−116.
(34) Sudarsanakumar, C.; Thomas, S.; Mathew, S.; Arundhathi, S.; Raj, D. R.; Prasanth, S.; Thomas, R. K. Selective Sensing of Curcumin Using L-Cysteine Derived Blue Luminescent Graphene Quantum Dots. *Mater. Res. Bull.* **2019**, *110*, 32−38.
(35) Wu, B.; Liu, X.; Shi, X.; Han, W.; Wang, C.; Jiang, L. Highly Photoluminescent and Temperature-Sensitive P, N, B-Co-Doped Carbon Quantum Dots and Their Highly Sensitive Recognition for Curcumin. *RSC Adv.* **2019**, *9*, 8340−8349.
(36) Zhao, X.; Li, F.; Zhang, Q.; Li, Z.; Zhou, Y.; Yang, J.; Dong, C.; Wang, J.; Shuang, S. Mn-Doped ZnS Quantum Dots with a 3-Mercaptopropionic Acid Assembly as a Ratiometric Fluorescence Probe for the Determination of Curcumin. *RSC Adv.* **2015**, *5*, 21504−21510.
(37) Yang, H.; Li, X.; Wang, X.; Chen, W.; Bian, W.; Choi, M. M. F. Silver-Doped Graphite Carbon Nitride Nanosheets as Fluorescent Probe for the Detection of Curcumin. *Luminescence* **2018**, *33*, 1062−1069.
(38) Zhou, D.; Li, D.; Jing, P.; Zhai, Y.; Shen, D.; Qu, S.; Rogach, A. L. Conquering Aggregation-Induced Solid-State Luminescence Quenching of Carbon Dots through a Carbon Dots-Triggered Silica Gelation Process. *Chem. Mater.* **2017**, *29*, 1779−1787.
(39) Wang, W.; Damm, C.; Walter, J.; Nacken, T. J.; Peukert, W. Photobleaching and Stabilization of Carbon Nanodots Produced by Solvothermal Synthesis. *Phys. Chem. Chem. Phys.* **2016**, *18*, 466−475.
(40) Penn, R. L.; Banpeld, J. F. Imperfect Oriented Attachment: Dislocation Generation in Defect Free Nanocrystals. *Science* **1998**, *281*, 969−971.
(41) Zhang, H.; Yang, D.; Ji, Y.; Ma, X.; Xu, J.; Que, D. Selenium Nanotubes Synthesized by a Novel Solution Phase Approach. *J. Phys. Chem. B* **2004**, *108*, 1179−1182.
(42) Ma, Y.; Qi, L.; Ma, J.; Cheng, H. Micelle-Mediated Synthesis of Single-Crystalline Selenium Nanotubes. *Adv. Mater.* **2004**, *16*, 1023−1026.
(43) Xi, G.; Xiong, K.; Zhao, Q.; Zhang, R.; Zhang, H.; Qian, Y. Nucleation-Dissolution-Recrystallization: A New Growth Mechanism for t-Selenium Nanotubes. *Cryst. Growth Des.* **2006**, *6*, 577−582.
(44) Lucovsky, G.; Mooradian, A.; Taylor, W.; Wright, G. B.; Keezer, R. C. Identification of the Fundamental Vibrational Modes of Trigonal, α - Monoclinic and Amorphous Selenium. *Solid State Commun.* **1967**, *5*, 113−117.
(45) Song, J.-M.; Zhu, J.-H.; Yu, S.-H. Crystallization and Shape Evolution of Single Crystalline Selenium Nanorods at Liquid-Liquid Interface: From Monodisperse Amorphous Se Nanospheres toward Se Nanorods. *J. Phys. Chem. B* **2006**, *110*, 23790−23795.
(46) Rubio, F.; Rubio, J.; Oteo, J. L. A DSC Study of the Drying Process of TEOS Derived Wet Silica Gels. *Thermochim. Acta* **1997**, *307*, 51−56.
(47) Tran, T. N.; Anh Pham, T. V.; Phung Le, M. L.; Thoa Nguyen, T. P.; Tran, V. M. Synthesis of Amorphous Silica and Sulfonic Acid Functionalized Silica Used as Reinforced Phase for Polymer Electrolyte Membrane. *Adv. Nat. Sci.: Nanosci. Nanotechnol.* **2013**, *4*, No. 045007.
(48) Bertoluzza, A.; Fagnano, C.; Antonietta Morelli, M.; Gottardi, V.; Guglielmi, M. Raman and Infrared Spectra on Silica Gel Evolving toward Glass. *J. Non-Cryst. Solids* **1982**, *48*, 117−128.
(49) Pol, V. G.; Srivastava, D. N.; Palchik, O.; Palchik, V.; Slifkin, M. A.; Weiss, A. M.; Gedanken, A. Sonochemical Deposition of Silver Nanoparticles on Silica Spheres. *Langmuir* **2002**, *18*, 3352−3357.
(50) Zhu, Y.-J.; Hu, X.-L. Preparation of Powders of Selenium Nanorods and Nanowires by Microwave-Polyol Method. *Mater. Lett.* **2004**, *58*, 1234−1236.
(51) Chen, Z.; Shen, Y.; Xie, A.; Zhu, J.; Wu, Z.; Huang, F. L-Cysteine-Assisted Controlled Synthesis of Selenium Nanospheres and Nanorods. *Cryst. Growth Des.* **2009**, *9*, 1327−1333.
(52) Dwivedi, C.; Shah, C. P.; Singh, K.; Kumar, M.; Bajaj, P. N. An Organic Acid-Induced Synthesis and Characterization of Selenium Nanoparticles. *J. Nanotechnol.* **2011**, *2011*, No. e651971.
(53) Li, H.; Song, X.; Yu, X.; Zhang, J.; Cui, Z.; Xue, Y.; Zhang, R. Preparation of Nano-t-Se with Different Particle Sizes and Particle Size Dependence of the Melting Thermodynamics. *CrystEngComm* **2019**, *21*, 5650−5657.
(54) Shah, C. P.; Singh, K. K.; Kumar, M.; Bajaj, P. N. Vinyl Monomers-Induced Synthesis of Polyvinyl Alcohol-Stabilized Selenium Nanoparticles. *Mater. Res. Bull.* **2010**, *45*, 56−62.
(55) Ma, Y.; Qi, L.; Shen, W.; Ma, J. Selective Synthesis of Single-Crystalline Selenium Nanobelts and Nanowires in Micellar Solutions of Nonionic Surfactants. *Langmuir* **2005**, *21*, 6161−6164.
(56) Ann Mary, K. A.; Unnikrishnan, N. V.; Philip, R. Ultrafast Optical Nonlinearity in Nanostructured Selenium Allotropes. *Chem. Phys. Lett.* **2013**, *588*, 136−140.
(57) Todorov, T. K.; Singh, S.; Bishop, D. M.; Gunawan, O.; Lee, Y. S.; Gershon, T. S.; Brew, K. W.; Antunez, P. D.; Haight, R. Ultrathin High Band Gap Solar Cells with Improved Efficiencies from the World's Oldest Photovoltaic Material. *Nat. Commun.* **2017**, *8*, No. 682.
(58) Andharia, E.; Kaloni, T. P.; Salamo, G. J.; Yu, S.-Q.; Churchill, H. O. H.; Barraza-Lopez, S. Exfoliation Energy, Quasiparticle Band Structure, and Excitonic Properties of Selenium and Tellurium Atomic Chains. *Phys. Rev. B* **2018**, *98*, No. 035420.
(59) Mary, K. A. A.; Unnikrishnan, N. V.; Philip, R. Role of Surface States and Defects in the Ultrafast Nonlinear Optical Properties of CuS Quantum Dots. *APL Mater.* **2014**, *2*, No. 076104.
(60) Khan, M. M.; Ansari, S. A.; Pradhan, D.; Han, D. H.; Lee, J.; Cho, M. H. Defect-Induced Band Gap Narrowed CeO_2 Nanostructures for Visible Light Activities. *Ind. Eng. Chem. Res.* **2014**, *53*, 9754−9763.
(61) Amani, M.; Lien, D.-H.; Kiriya, D.; Xiao, J.; Azcatl, A.; Noh, J.; Madhvapathy, S. R.; Addou, R.; Kc, S.; Dubey, M.; Cho, K.; Wallace, R. M.; Lee, S.-C.; He, J.-H.; Ager, J. W.; Zhang, X.; Yablonovitch, E.; Javey, A. Near-Unity Photoluminescence Quantum Yield in MoS2. *Science* **2015**, *350*, 1065−1068.
(62) Wang, S.; Meng, X.; Das, A.; Li, T.; Song, Y.; Cao, T.; Zhu, X.; Zhu, M.; Jin, R. A 200-Fold Quantum Yield Boost in the Photoluminescence of Silver-Doped AgxAu25−x Nanoclusters: The 13 Th Silver Atom Matters. *Angew. Chem.* **2014**, *126*, 2408−2412.

https://doi.org/10.1021/acsomega.1c02441
ACS Omega 2021, 6, 21525−21533

(63) Wang, H.; Zhang, C.; Rana, F. Ultrafast Dynamics of Defect-Assisted Electron−Hole Recombination in Monolayer MoS2. *Nano Lett.* **2015**, *15*, 339−345.
(64) Zheng, M.; Xie, Z.; Qu, D.; Li, D.; Du, P.; Jing, X.; Sun, Z. On−Off−On Fluorescent Carbon Dot Nanosensor for Recognition of Chromium(VI) and Ascorbic Acid Based on the Inner Filter Effect. *ACS Appl. Mater. Interfaces* **2013**, *5*, 13242−13247.
(65) Yu, C.; Zhuang, Q.; Cui, H.; Li, L.; Ding, Y.; Lin, J.; Duan, Y. A Fluorescent "Turn-off" Probe for the Determination of Curcumin Using Upconvert Luminescent Carbon Dots. *J. Fluoresc.* **2020**, *30*, 1469−1476.
(66) Duan, Z.; Yin, M.; Zhang, C.; Song, G.; Zhao, S.; Yang, F.; Feng, L.; Fan, C.; Zhu, S.; Wang, H. Polyhydric Polymer-Loaded Pyrene Composites as Powerful Adsorbents and Fluorescent Probes: Highly Efficient Adsorption and Test Strips-Based Fluorimetric Analysis of Curcumin in Urine and Plant Extracts. *Analyst* **2018**, *143*, 392−395.
(67) Guo, Z.; Zhu, Z.; Sun, Z.; Zhang, X.; Chen, Y. Synthesis of Dual-Emitting (Gd,Eu)2O3-PEI@CD Composite and Its Potential as Ratiometric Fluorescent Sensor for Curcumin. *Mater. Res. Bull.* **2018**, *108*, 83−88.
(68) Han, Z.; Zhang, H.; He, L.; Pan, S.; Liu, H.; Hu, X. One-Pot Hydrothermal Synthesis of Nitrogen and Sulfur Co-Doped Carbon Dots and Their Application for Sensitive Detection of Curcumin and Temperature. *Microchem. J.* **2019**, *146*, 300−308.
(69) Zheng, B.; Zhang, X.; Peng, S.; McClements, D. J. Impact of Curcumin Delivery System Format on Bioaccessibility: Nanocrystals, Nanoemulsion Droplets, and Natural Oil Bodies. *Food Funct.* **2019**, *10*, 4339−4349.
(70) Sahoo, N. K.; Jana, G. C.; Aktara, M. N.; Das, S.; Nayim, S.; Patra, A.; Bhattacharjee, P.; Bhadra, K.; Hossain, M. Carbon Dots Derived from Lychee Waste: Application for Fe3+ Ions Sensing in Real Water and Multicolor Cell Imaging of Skin Melanoma Cells. *Mater. Sci. Eng. C* **2020**, *108*, No. 110429.

https://doi.org/10.1021/acsomega.1c02441
ACS Omega 2021, 6, 21525−21533